Mechanics & Industry **21**, 403 (2020)
© AFM, EDP Sciences 2020
https://doi.org/10.1051/meca/2020030

Mechanics & Industry

Available online at:
www.mechanics-industry.org

REGULAR ARTICLE

Kinematic design of a hybrid planar-tripod mechanism for bone reduction surgery

Terence Essomba* and Sinh Nguyen Phu

Department of Mechanical Engineering, National Central University, No. 300, Zhongda Rd., Zhongli District, Taoyuan City 32001, Taiwan

Received: 14 February 2019 / Accepted: 30 March 2020

Abstract. In the most severe cases of longitudinal bone fractures such as femur, tibias, humerus etc., the bone can be completely separated into two fragments. In order to guarantee the re-ossification of the bone, it is required to reposition the bone fragments together. This process requires a delicate surgery called "bone reduction surgery". The most advanced technique relies on the use of a robotic manipulator to reposition the bone fragments with higher precision and stability than manual surgeries. The present work introduces the kinematic design of a new hybrid mechanical architecture to perform this task. It is composed of a 3-PRP planar mechanism attached with a 3-RPS tripod mechanism. The kinematic analysis of this mechanism is provided while taking account the tripod parasitic motion. Kinematic simulations using Matlab and Adams are performed to validate the kinematic and velocity models and the parasitic motion compensation provided by the planar mechanism. The workspace of this hybrid mechanism is then compared to the standard hexapod mechanism that is widely used in bone reduction surgery. It reveals that the proposed mechanism can generate a larger workspace with the same linkage dimensions.

Keywords: bone reduction surgery / planar mechanism / tripod mechanism / kinematic simulation / workspace

1 Introduction

In Human anatomy, longitudinal bones are more exposed to fractures due to their location and longitudinal geometry, such as limb bones. According to medical data history, the femur has the highest involvement rate in fracture with around 37 per 100,000 people per year [1,2]. Some fracture cases require a specific type of surgery before recovering, namely bone reduction surgery. In most critical cases, the fractured bone is totally separated into two pieces [3]. In bone reduction surgery, the bones fragments are relocated in their original position. During this surgical procedure, a large incision must be performed on the patient to allow a physical access to the bone fragments. Once accessible, the surgeons will manually displace the bone fragments to their original configuration before fixation using specific prosthesis, as shown in Figure 1. One major problem of this technique is that surgeons have to use a considerable amount of physical strength to relocate to bones because of the natural recall force applied by the patient's anatomy (muscular tissues and tendons). The force applied by the surgeon must counter the force exerted by the patient's tissues attached with the bone. Later, the minimally invasive reduction surgery has been developed in order to minimize the risk associated to "open surgery" (bleeding, infection). A series of nails are inserted into the bone fragments, which requires incisions no larger than the nails sectional dimensions (a few millimeters). The repositioning is then performed by manipulating these nails [4]. Although this technique represents less risk for the patient, a higher level of dexterity is required from the surgeon since there is no direct vision of the broken bone.

Consequently, their position is monitored with intra-operative images during the operation. The surgeon will then adjust the position of the bone pieces based on the real time images received. But minimally invasive reduction surgeries is still performed using high strength to reposition the bones. And when surgical implants are required, the bones must the maintained in position the time the implant is fixed. Also, the stress generated by the muscular tissues will always cause a residual motion of the bones parts when they are released. A misalignment between the bones and the implants can therefore occur after their installation. The hazard environment of image-guided surgery is also a critical issue to consider. Indeed, while surgeons must

* e-mail: tessomba@cc.ncu.edu.tw

Fig. 1. Fracture of a patient's femur (a). Result of reduction surgery and implant installation (b).

perform these adjustments, both surgeons and patients are subject to excessive X-ray exposure during the procedure. But unlike patients, surgeons will suffer from repeated exposures to the radiation generated by the medical imaging system.

To solve the problems associated with manual bone reduction surgery (both opened and minimally invasive), the use of mechanism has been proposed. The technique relies on fixing the mechanism base and end effector respectively to two different fragments of one bone. Pending on its architecture, the mechanism will generate of a motion between its base and its end effector when its joints are operated. By extension, a motion is then performed between one bone piece and the other. It is therefore possible to control the motion of the bone fragments by operating the mechanism joints. Performing a complete bone reduction requires the manipulation of one of the bone fragments by moving it along three linear directions and rotating it around three different axes. Therefore, a mechanism dedicated to bone reduction surgery should generate a total of six Degrees of Freedom (DoF): three linear DoF and 3 angular DoF as a major requirement. During the pre-operative phase, the surgeon will observe the pre-operative images of the patient fracture and will estimate an appropriate trajectory for the bones repositioning. The trajectory is defined considering two main concerns: guarantying an accurate fracture surface matching and avoiding collision between the structures of the bone fragments before the final approach. During the intra-operative phase, the surgeon will approximatively generate the planned trajectory. The evolution of the trajectory and the final matching are verified visually based on the intra-operative medical images. An advantageous characteristic is the ability to

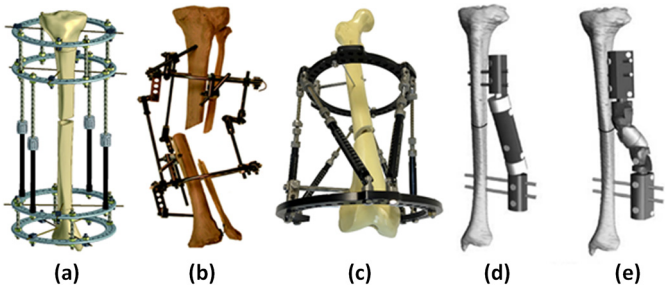

Fig. 2. External fixators: (a) Ilizarov apparatus; (b) Ortho-SUV Frame; (c) Taylor Spatial Frame; (d) Orthofix fixator; (e) Dynafix fixator.

rotate the bone fragment along its longitudinal axis in order to improve the fracture surface matching between the two fragments. On addition, it is important that this angle can maintain a range of values as large as possible while the mechanism end effector moves away the center of its workspace. Meaning that once the bone fractured bone are almost repositioned, it is necessary that the mechanism has a range of longitudinal rotation large enough to ascertain a correct surface matching. In the literature, several research works can be found. If the focus is given on mechanism concept, the literature review of robotic bone reduction surgery can be divided in several categories. Fully embedded architectures are presented as serial or parallel structures that are connected to the patient's anatomy by both their base and end effector. In the case of deported mechanisms, only their end effector is connected to the patient's bone.

The first mechanism assisting bone reduction surgery has been reported in 1992. Dr. Gavril Abramovich Ilizarov developed the first circular external fixator with cross wires, named Ilizarov, for complex bone fractures [5]. The Ilizarov external fixator shown in Figure 2a, consists in two or more rings that are connected each other by four threaded rods with adjustable nuts. This fixator was patented and accepted for clinical application. In 1999, an advanced version of the Ilizarov fixator has been introduced and successfully tested on 16 patients presenting fracture of the tibia [6]. The mechanism used was composed of two cylindrical modules that are connected by a hexapod mechanism of 6 legs and 12 spherical joints. These cylindrical modules are commercially available. That mechanical architecture is able to displace one cylinder with 6 DoF from the other. Each fixator is mounted on one bone fragment by surrounding the patient's limb. One disadvantage of the Ilizarov fixator is that the completion of bone reduction cannot be achieved in one-time adjustment in complex fractures. It is required to modify or change the configuration of frame during several correction procedures. Also, the adjustment of one component of the fixator might cause the displacement of the others and therefore additional reassembly steps will be needed for correctly positioning bone segments. Hence, it can cause inaccurate and time-consuming corrections.

In order to overcome this problem, a software-based Ortho-SUV Frame (OSF) for fractures with single step

solution has been developed by Ortho-SUV Ltd in 2006. As illustrated in Figure 2b, the OSF frame consists in one base and one mobile rings that are connected to each other by six telescopic struts equipped with scales. A computer program is used to calculate the length of struts for fracture reduction in a single stage. This fixator has the advantage of better accuracy, higher rigidity and shorter correction time in comparison with the Ilizarov apparatus [7,8].

Since then, the concept of fully embedded robotic manipulators has been widely used for robotically assisted reduction surgery of longitudinal bones. In 2004, another hexapod has been used for bone reduction surgery [9]. A manually adjusted hexapod has been designed to manipulate two fixation arcs attached to each piece of the bone. A specific software was developed to allow the control of 6 DoF. The prototype has successfully performed the fracture reduction of four patient. The Taylor Spatial Frame (TSF) shown in Figure 2c, is another hexapod mechanism that is widely used in reduction. It was introduced by Charles and Harold Taylor in 1999. This device was used for the first operation in 1995 and patented in 1997 [10]. The standard TSF is composed of two full or partial rings connected by six telescopic struts through multi-axial joints at each end. It enables a 6-DoF manipulation by adjusting six struts so this frame. Compared to Ilizarov fixator and unilateral devices, the TSF fixator offers more accurate results and less complicated modifications of the frame during surgery. Additionally, a variety of proposed 6-DOF parallel fixators have been proposed by modifying the Ilizarov apparatus or TSF fixator such as ILD1, ILD2 Ilizarov-like fixations, into hexapod devices [11,12]. In 2006, a simplified version of the TSF has been proposed for bone reduction [13]. A study has been reported about the use of the device on 10 pediatric patients from 8 to 15 years [14]. The same mechanical architecture has been used for the implementation of a computer-assisted orthopaedic procedure based on 3D CT-Scan image in 2012. It was tested on the fracture reduction of 10 bovine femurs. A similar hexapod mechanism was designed and experimented for fracture reduction of longitudinal bones [15]. They also developed a program for the 3-D reconstructing of models from DICOM-format CT images to improve the accuracy of surgery. Ten experiments using this system on bovine femoral fractures have been carried out. As results, this system can provide simultaneous rotations and translations in all directions and it allows efficient and accurate fracture reduction. A removable hybrid mechanism for long bone fracture reduction has been developed [16]. This mechanism has two units: one reduction unit based on 6-DoF Stewart platform and one fixing unit. The fractures were attached to two parts of the fixing unit. Then they were connected to the two platforms of the reduction unit. The relative motion between two platforms of the fixing unit was controlled by six hydraulic legs. In 2017, a new 6-DoF parallel robot with three legs for long-bone fracture reduction has been proposed [17]. Each RPS leg is equipped one prismatic actuator and one rotary actuator. This architecture has much larger dexterous and rotational workspace in comparison to the well-known six prismatic legs Stewart platform.

Other types of mechanical architectures for bone reduction surgery can be found in the literature. Embedded serial robots are still fully embedded into the patient's anatomy but they rely on serial architectures. Dynafix and Orthofix fixators, respectively shown in Figure 2d and e, are known to belong to this category [18–21]. Bone reduction surgery can be performed using another concept of mechanism that is referred to as "deported" mechanism. By "deported" mechanism, it is understood that while the mechanism end effector is still fixed with the patient's anatomy (bone piece), its base is attached to an external reference. Several manipulators have been reported in this category [22–26].

According to the literature review of mechanisms and robotic systems for bone reduction surgery, several conclusions can be made about this topic:

– Existing bone reduction robotic systems are limited in diversity. Although they can be regrouped in three conceptual categories, only three main types of mechanical architectures can be reported.
– The recent emergence of hybrid architectures seems to bring a certain contribution to this specific surgical application in terms of workspace [17].

The recent literature review tends to highlight hybrid mechanisms combining parallel architectures, which seem destined to promising outcomes. Parallel mechanical architectures offer higher stiffness, higher accuracy, higher payload and low inertia in comparison to serial architectures. But they provide smaller workspace than serial ones. For example, the Stewart platform that is a standard in bone reduction surgery, has several advantageous characteristics, including high stiffness, precision and high load to weight ratio, while having 6 DoF (3 angular and 3 linear). But the workspace of this architecture appears to be limited. Its range of angular motion is greatly reduced as the end effector moves away from the workspace center. Also, its ability to rotate the bone around its longitudinal axis is very limited, while this feature is important feature for ascertain the surface correspondence of bone fragments. For this reason, some scholars tried to design new types of hybrid architectures by combining the advantage of several structures. The present work uses this strategy by proposing hybrid mechanical architecture for bone reduction surgery. In robotic assisted bone reduction surgery, very few reported research deals with the kinematic aspect of associated with this surgical application. The main contribution of the present research is to propose a mechanical architecture which kinematic is specifically adapted to bone reduction surgery. The next Section introduces and defines the new hybrid planar-tripod mechanism. Its kinematic model and velocity models are studied in Section 3. A series of kinematic simulation validate this study in Section 4. The Section 5 proposes the workspace analysis of this mechanism and a comparison with a standard architecture. And the last Section is dedicated to the conclusion.

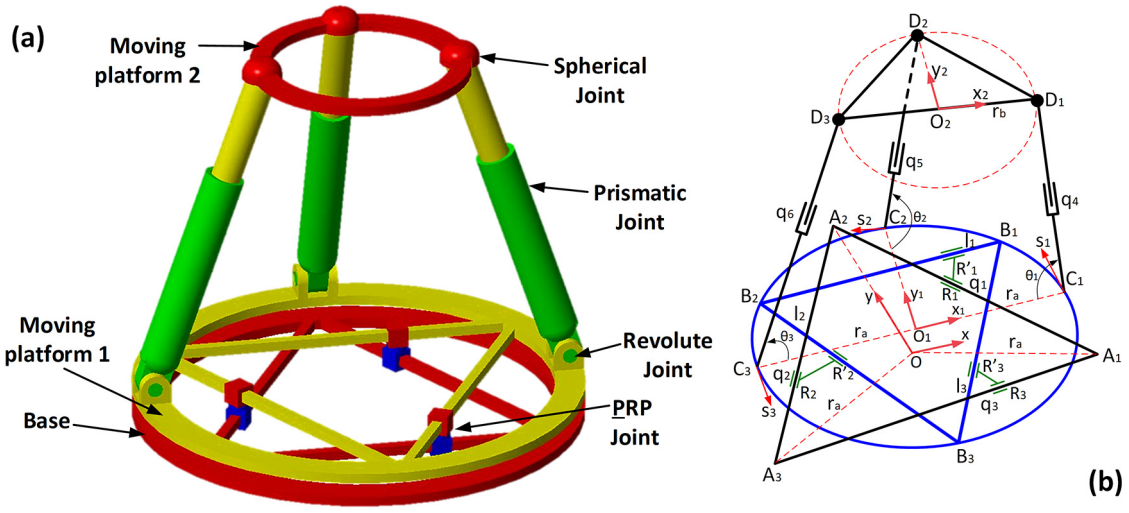

Fig. 3. Hybrid planar-tripod mechanism (a). Kinematic drawing of the mechanism (b).

2 Presentation of the hybrid planar-tripod architecture

In this study, the proposed hybrid mechanism is a combination of two different parallel architecture. It consists of one planar parallel mechanism and one spatial tripod mechanism that are connected in series as illustrated in Figure 3a. The planar parallel mechanism is a double triangular architecture that has been introduced by Daniali et al. in 1993 [27]. It has two triangular platforms: one is fixed and considered as the architecture base and one is a movable platform. The mobile platform is connected to the fixed platform by three PRP legs. Each of them has one active prismatic joint attached to the edge of fixed triangular platform and one passive prismatic joint attached on the edge of mobile triangular platform. Both prismatic joints are linked by a passive revolute joint. This planar mechanism provides two linear DoF and one angular DoF. The mechanism fixed on the planar mechanism mobile platform is made of a tripod architecture. This 3-RPS parallel mechanism was introduced by Hunt in 1983 [28]. It also has two platforms; one is considered as the base and one is a mobile platform that is manipulated with two angular DoF and one linear DoF. Both platforms are connected together by the three RPS legs. Each leg is connected to the fixed platform by a passive revolute joint and to the mobile platform a passive spherical joint. These two passive joints are linked be an active prismatic joint. The three RPS leg of the tripod are disposed as an isosceles triangle. This architectural disposition has been chosen in order to suppress the parasitic motion on one axis. By connecting these two 3-DoF mechanisms in series, a hybrid parallel-parallel manipulator is created with a total of six DoF: three linear and three angular. Compared with well-known Stewart platform, this robot has simpler kinematics and control design. One major advantage over the Stewart platform is its capacity to generate a much larger range of longitudinal rotation which will improve the practice of bone reduction surgery.

As shown in Figure 3b, the original reference frame $\{\mathrm{O}\mathbf{xyz}\}$ is attached with the base of the planar mechanism, and the point O is located at the center of the equilateral triangle $\mathrm{A_1A_2A_3}$ that forms this base. It is dimensioned by the radius r_a of its circum circle. The $\mathbf{x}$ axis is parallel to line $\mathrm{A_1A_3}$, the $\mathbf{y}$ axis pointing toward the $\mathrm{A_2}$ and the $\mathbf{z}$ axis is perpendicular to the base plane. Another reference frame $\{\mathrm{O_1}\mathbf{x_1y_1z_1}\}$ is attached to the planar mechanism moving platforms, namely the mobile platform 1 (MP1), that is represented by the equilateral triangle $\mathrm{B_1B_2B_3}$. This triangle is assumed to have the same size as $\mathrm{A_1A_2A_3}$ and is also dimensioned by r_a. The point $\mathrm{O_1}$ coincides the center of $\mathrm{B_1B_2B_3}$, the $\mathbf{x_2}$ axis is parallel to $\mathrm{B_1B_2}$, the $\mathbf{y_2}$ axis is directed to $\mathrm{B_1}$ but pointing toward the opposition direction and the $\mathbf{z_2}$ axis is perpendicular to the PM1 plane. At the same time, reference frame $\{\mathrm{O_1}\mathbf{x_1y_1z_1}\}$ is also attached to the base of the tripod mechanism. It is represented by an isosceles triangle $\mathrm{C_1C_2C_3}$ which circumcircle radius is also given by r_a. The passive revolute joints of tripod RPS legs are located at the corners of this triangle. Therefore, the point $\mathrm{O_1}$ is located at the center of $\mathrm{C_1C_3}$, the $\mathbf{x_1}$ axis is collinear with $\mathrm{C_1C_3}$ and is pointing toward $\mathrm{C_1}$, the $\mathbf{y_1}$ axis is pointing toward $\mathrm{C_2}$ and the $\mathbf{z_2}$ axis is perpendicular to the tripod base plane. Similarly, the third reference frame $\{\mathrm{O_2}\mathbf{x_2y_2z_2}\}$ is attached to the mobile platform of the tripod, namely the mobile platform 2 (MP2) which is the end effector of the entire planar-tripod mechanism. The passive spherical joint of all RPS legs is located at $\mathrm{D_k}$ ($k = 1$, 2, 3). The point $\mathrm{O_2}$ is located at the center the isosceles triangle $\mathrm{D_1D_2D_3}$ that represents the MP2. Its dimension is given by the radius r_b of its circumcircle. The $\mathbf{x_2}$ axis is directed to $\mathrm{D_1}$, the $\mathbf{y_2}$ axis to $\mathrm{D_2}$ and the $\mathbf{z_2}$ axis is normal to the triangle plane.

The planar and tripod mechanisms are both actuated by prismatic joints. On the planar mechanism, the position of the active prismatic joints $\mathrm{R_1}$, $\mathrm{R_2}$ and $\mathrm{R_3}$ is measured by their distance from their associated corners $\mathrm{A_1}$, $\mathrm{A_2}$ and $\mathrm{A_3}$ respectively. The corresponding input variables q_1, q_2 and q_3 are therefore defined. On the tripod mechanism, the variable θ_k measures the inclination of the RPS legs by

giving the angles ($O_1C_kD_k$), with $k = 1, 2, 3$. The input variables q_4, q_5 and q_6 generated by the active prismatic joints measure the distance between C_1D_1, C_2D_2 and C_3D_3 respectively.

3 Kinematic analysis of the hybrid mechanism

The main advantage of this architecture is that the motion of the two moving platforms can be addressed separately when studying the kinematic and velocity models. But a particular attention must be given the effect of the parasitic motion generated by the tripod mechanism.

3.1 Inverse kinematic model

The inverse kinematic model of the presented mechanism can be solved in several steps. The first step consists in analyzing separately the kinematic of two mechanism: the 3-PRP planar mechanism and the 3-RPS tripod. In the second step, the kinematic of the tripod must be expressed in the reference frame of the entire mechanism base. Another step consists in compensating the parasitic motion of the tripod.

First, the inverse kinematics of the triangular planar parallel mechanism is presented. In other words, the position and orientation of the MP1 in the origin reference frame {O**xyz**} are studied. The double triangular manipulator has 3-DoF: two translations along **x** and **y** axes and one rotation about the **z** axis. The linear position of the MP1 is defined by the vector $\mathbf{o_1} = [x_1\ y_1\ 0]$ expressed in the fixed frame {O**xyz**} and its angular position is designed by the rotation angle γ_1 about the **z** axis. It is assumed that there is no distance between the MP1 and the base along the vertical axis. As shown in Figure 3b, the position vectors $\mathbf{r_1}$, $\mathbf{r_2}$ and $\mathbf{r_3}$ of the active prismatic joints R_1, R_2, and R_3 are expressed in the fixed reference frame {O**xyz**} as followed:

$$\mathbf{r}_1 = \begin{bmatrix} \frac{\sqrt{3}}{2}r_a - \frac{1}{2}q_1 \\ -\frac{1}{2}r_a + \frac{\sqrt{3}}{2}q_1 \\ 0 \end{bmatrix}, \quad \mathbf{r}_2 = \begin{bmatrix} -\frac{1}{2}q_2 \\ r_a - \frac{\sqrt{3}}{2}q_2 \\ 0 \end{bmatrix},$$
$$\mathbf{r}_3 = \begin{bmatrix} -\frac{\sqrt{3}}{2}r_a + q_3 \\ -\frac{1}{2}r_a \\ 0 \end{bmatrix}. \tag{1}$$

With r_a, the radius of the circumcircle of center O passing by A_1, A_2, and A_3.

Assuming that $l_k\,(k = 1, 2, 3)$ is the distance between the corner B_k of the moving equilateral triangle $B_1B_2B_3$ and the closest passive prismatic joints R'_k, namely $B_1R'_1$, $B_2R'_2$ and $B_3R'_3$ respectively, then the position vector of the passive prismatic joints R'_k are expressed in the mobile frame $\{O_1\mathbf{x_1y_1z_1}\}$ as followed:

$${}^1\mathbf{r}'_1 = \begin{bmatrix} \frac{\sqrt{3}}{2}r_a - l_1 \\ \frac{1}{2}r_a \\ 0 \end{bmatrix}, \quad {}^1\mathbf{r}'_2 = \begin{bmatrix} -\frac{\sqrt{3}}{2}r_a + \frac{1}{2}l_2 \\ \frac{1}{2}r_a - \frac{\sqrt{3}}{2}l_2 \\ 0 \end{bmatrix},$$
$${}^1\mathbf{r}'_3 = \begin{bmatrix} \frac{1}{2}l_3 \\ \frac{\sqrt{3}}{2}l_3 - r_a \\ 0 \end{bmatrix}. \tag{2}$$

In the fixed frame {O**xyz**}, the position of the passive prismatic joints R'_k are calculated as following:

$$\mathbf{r}'_k = \boldsymbol{O}_1 + \mathbf{R}_z(\gamma_1)\cdot{}^1\mathbf{r}'_k \tag{3}$$

where $\mathbf{R_z}(\gamma_1)$ is the rotation matrix of angle γ_1 about **z** axis.

Because the active prismatic joints R_k on the base are attached the passive prismatic joints R'_k by a revolute joint as depicted in Figure 3b, the x and y coordinates of the two prismatic joints R_k and R'_k in the fixed frame are same.

Which gives the following constraint:

$$\begin{cases} \boldsymbol{r}_{kx} = \boldsymbol{r}'_{kx} \\ \boldsymbol{r}_{ky} = \boldsymbol{r}'_{ky} \end{cases}. \tag{4}$$

After developing the expression given by equation (4), the prismatic input coordinates q_k (with $k = 1, 2, 3$) are isolated and expressed as followed:

See equation (5) below.

where $s(.)$ and $c(.)$ are respectively equal to sin(.) and cos (.).

Next, the position and orientation the MP2 in the moving reference frame $\{O_1\mathbf{x_1y_1z_1}\}$ attached to the MP1 are presented. The 3-RPS parallel mechanism is a special lower-mobility parallel mechanism that has parasitic motions between the MP2 and the MP1 [29]. In order to define these parasitic motions, the vector ${}^1\mathbf{o_2} = [x_2\ y_2\ z_2]^T$ is assumed to be pointing the end effector O_2 and is expressed in the reference frame $\{O_1\mathbf{x_1y_1z_1}\}$. Its orientation Yaw-Pitch-Roll are given by the angles (γ_2, β_2, α_2) respectively rotating about $\mathbf{z_1}$, $\mathbf{y_1}$, and $\mathbf{x_1}$ axis. The rotation matrix describing the orientation of the reference frame attached

$$\begin{cases} (s\gamma_1 + \sqrt{3}c\gamma_1)q_1 = r_a + (\sqrt{3}r_a - 2x_1)s\gamma_1 + (r_a + 2y_1)c\gamma_1 \\ (s\gamma_1 + \sqrt{3}c\gamma_1)q_2 = r_a + (\sqrt{3}r_a + x_1 - \sqrt{3}y_1)s\gamma_1 + (r_a - \sqrt{3}x_1 - y_1)c\gamma_1 \\ (s\gamma_1 + \sqrt{3}c\gamma_1)q_3 = r_a + (\sqrt{3}r_a + x_1 + \sqrt{3}y_1)s\gamma_1 + (r_a + \sqrt{3}x_1 - y_1)c\gamma_1 \end{cases} \tag{5}$$

to the MP2 can be written as:

$$ {}^{1}_{2}\mathbf{R} = \mathbf{R_z}(\gamma_2)\mathbf{R_y}(\beta_2)\mathbf{R_x}(\alpha_2). \tag{6} $$

The position vectors of spherical joints D_1, D_2, D_3 are expressed in the coordinate system $\{O_2\mathbf{x_2y_2z_2}\}$ of the MP2 as followed:

$$ {}^{2}\mathbf{d}_1 = \begin{bmatrix} r_b \\ 0 \\ 0 \end{bmatrix}, \quad {}^{2}\mathbf{d}_2 = \begin{bmatrix} 0 \\ r_b \\ 0 \end{bmatrix}, \quad {}^{2}\mathbf{d}_3 = \begin{bmatrix} -r_b \\ 0 \\ 0 \end{bmatrix}. \tag{7} $$

From Figure 3b, the position vector of the spherical joints D_1, D_2, D_3 in the frame $\{O_1\mathbf{x_1y_1z_1}\}$ is calculated:

$$ {}^{1}\boldsymbol{d}_k = {}^{1}\boldsymbol{o}_2 + {}^{1}_{2}\mathbf{R}.\,{}^{2}\boldsymbol{d}_k. \tag{8} $$

With $k = 1, 2, 3$. On the other hand, the mechanical constraints of the revolute joints C_k $(k = 1, 2, 3)$ impose the following system of equation:

$$ \begin{cases} {}^{1}\boldsymbol{d}_{1y} = 0 \\ {}^{1}\boldsymbol{d}_{2x} = 0 \\ {}^{1}\boldsymbol{d}_{3y} = 0. \end{cases} \tag{9} $$

By solving the systems of equations given by equation (9), the parasitic motions can be obtained as:

$$ \begin{cases} \gamma_2 = 0 \\ x_2 = -r_b s\alpha_2 s\beta_2\,. \\ y_2 = 0 \end{cases} \tag{10} $$

According to equation (10), the parasitic motion generated by the 3-RPS architecture only affects the x component of the end effector position on the tripod reference frame. In other words, the linear position of the end-effector O_2 in the horizontal plane of the fixed reference frame will be composed of the linear motion of the MP1 and a unidirectional parasitic motion along the x_2 axis.

Finally, the inverse kinematic model of the proposed parallel mechanism will be obtained by coupling the motion of the two parallel mechanisms. The parasitic motion of the tripod mechanism relative to the first moving platform will be compensated by the linear motion of the triangular mechanism. The Cartesian coordinates of the end-effector O_2 expressed in the reference frame $\{O\mathbf{xyz}\}$ are given by $\mathbf{o_2} = [x\ y\ z]^{\mathrm{T}}$ and its orientation is presented by Yaw, Pitch, Roll angles (γ, β, α).

$$ {}^{0}_{2}\mathbf{R} = \mathbf{R}_z(\gamma)\mathbf{R}_y(\beta)\mathbf{R}_x(\alpha) = \begin{bmatrix} r_{11} & r_{12} & r_{13} \\ r_{21} & r_{22} & r_{23} \\ r_{31} & r_{32} & r_{33} \end{bmatrix} \tag{11} $$

The Cartesian coordinate of spherical joint D_1, D_2, D_3 in the reference frame $\{O\mathbf{xyz}\}$ is given as followed:

$$ \mathbf{d}_k = \mathbf{o}_2 + {}^{0}_{2}\mathbf{R}.\,{}^{2}\mathbf{d}_k \tag{12} $$

By developing equation (12), the position vector of spherical joints D_1, D_2, D_3 expressed in the reference frame $\{O_1\mathbf{x_1y_1z_1}\}$ of the moving platform 1 are written as:

$$ {}^{1}\mathbf{d}_1 = \begin{bmatrix} r_a - q_4 c\theta_1 \\ 0 \\ q_4 s\theta_1 \end{bmatrix}, \quad {}^{1}\mathbf{d}_2 = \begin{bmatrix} 0 \\ r_a - q_5 c\theta_2 \\ q_5 s\theta_2 \end{bmatrix}, $$
$$ {}^{1}\mathbf{d}_3 = \begin{bmatrix} q_6 c\theta_3 - r_a \\ 0 \\ q_6 s\theta_3 \end{bmatrix} \tag{13} $$

where q_4, q_5 and q_6 are the length of the tripod legs C_1D_1, C_2D_2, C_3D_3 respectively and θ_1, θ_2 and θ_3 are the rotation angle of the tripod legs. The position vector of spherical joints D_1, D_2, D_3 in the coordinate system $\{O\mathbf{xyz}\}$ is written as:

$$ \mathbf{d}_k = \mathbf{o}_1 + \mathbf{R}_z(\gamma).\,{}^{1}\mathbf{d}_k \tag{14} $$

Solving equation (12) into equation (13), yields the following system of equations:

$$ \begin{cases} x_1 + c\gamma(r_a - q_4 c\theta_1) = x + r_{11}{\cdot}r_b \\ y_1 + s\gamma(r_a - q_4 c\theta_1) = y + r_{21}{\cdot}r_b \\ x_1 - s\gamma(r_a - q_5 c\theta_2) = x + r_{12}{\cdot}r_b \\ y_1 + c\gamma(r_a - q_5 c\theta_2) = y + r_{22}{\cdot}r_b \\ x_1 + c\gamma(-r_a + q_6 c\theta_3) = x - r_{11}{\cdot}r_b \\ y_1 + s\gamma(-r_a + q_6 c\theta_3) = y - r_{21}{\cdot}r_b \end{cases} \tag{15} $$

Equation (15) is then written into a matrix form as followed:

$$ \mathbf{o}_1 = \begin{bmatrix} x_1 \\ y_1 \\ z_1 \end{bmatrix} = \begin{bmatrix} x + r_b \sin(\alpha)\sin(\beta)\cos(\gamma) \\ y + r_b \sin(\alpha)\sin(\beta)\sin(\gamma) \\ 0 \end{bmatrix}. \tag{16} $$

As the previous explanation, the Yaw rotation of the second moving platform is the same as the Yaw angle of the first moving platform. Therefore, the input coordinates q_k $(k = 1, 2, 3)$ can be obtained by substituting equation (16) into equation (6) and are written as:

See equation (17) below.

The position vectors of revolute joints C_k $(k = 1, 2, 3)$ in the coordinate system $\{O_1\mathbf{x_1y_1z_1}\}$ are given

$$ \begin{cases} q_1 = \dfrac{r_a + r_a c\gamma + 2yc\gamma - 2xs\gamma + \sqrt{3}r_a s\gamma}{s\gamma + \sqrt{3}c\gamma} \\ q_2 = \dfrac{r_a + r_a c\gamma + \sqrt{3}r_a s\gamma - yc\gamma + xs\gamma - \sqrt{3}ys\gamma - \sqrt{3}xc\gamma - \sqrt{3}r_b s\alpha s\beta}{s\gamma + \sqrt{3}c\gamma} \\ q_3 = \dfrac{r_a + r_a c\gamma + \sqrt{3}r_a s\gamma - yc\gamma + xs\gamma + \sqrt{3}ys\gamma + \sqrt{3}xc\gamma + \sqrt{3}r_b s\alpha s\beta}{s\gamma + \sqrt{3}c\gamma} \end{cases} \tag{17} $$

as followed:

$$ {}^1\mathbf{c}_1 = \begin{bmatrix} r_a \\ 0 \\ 0 \end{bmatrix}, \quad {}^1\mathbf{c}_2 = \begin{bmatrix} 0 \\ r_a \\ 0 \end{bmatrix}, \quad {}^1\mathbf{c}_3 = \begin{bmatrix} -r_a \\ 0 \\ 0 \end{bmatrix} \tag{18} $$

The position vector of revolute joints C_k ($k=1, 2, 3$) in the coordinate system {O**xyz**} is written as:

$$ \mathbf{c_k} = \mathbf{o}_1 + \mathbf{R}_z(\gamma).{}^1\mathbf{c}_k \tag{19} $$

The length of the active prismatic joints q_{k+3} ($k=1, 2, 3$) of the tripod mechanism can then be determined by the following equation:

$$ \begin{aligned} q_{k+3} &= \|C_kD_k\| = \|\mathbf{d}_k - \mathbf{c_k}\| \\ &= \|\mathbf{o}_2 + {}^0_2\mathbf{R}.{}^2\mathbf{d}_k - \mathbf{o}_1 - \mathbf{R}_z(\gamma).{}^1\mathbf{c}_k\| \end{aligned} \tag{20} $$

Developing equation (20) leads to:

$$ \begin{cases} q_4 = \sqrt{(z - r_b s\beta)^2 + (r_a - r_b c\beta + r_b s\alpha s\beta)^2} \\ q_5 = \sqrt{(z + r_b s\alpha c\beta)^2 + (r_a - r_b c\alpha)^2} \\ q_6 = \sqrt{(z + r_b s\beta)^2 + (r_a - r_b c\beta - r_b s\alpha s\beta)^2} \end{cases} \tag{21} $$

3.2 Velocity model

As the presented mechanism is a parallel architecture, it is expected that its velocity model, i.e. the relationship between the joint input velocities and end effector velocity, will be expressed as:

$$ \mathbf{A} \times \begin{bmatrix} \dot{q}_1 \\ \dot{q}_2 \\ \dot{q}_3 \\ \dot{q}_4 \\ \dot{q}_5 \\ \dot{q}_6 \end{bmatrix} = \mathbf{B} \times \begin{bmatrix} \dot{x} \\ \dot{y} \\ \dot{z} \\ \dot{\alpha} \\ \dot{\beta} \\ \dot{\gamma} \end{bmatrix} \tag{22} $$

By differentiating equation (17) with the time, the velocity model of the double triangular mechanical architecture can be written in a matrix form as followed:

$$ \mathbf{J_A} \times \begin{bmatrix} \dot{q}_1 \\ \dot{q}_2 \\ \dot{q}_3 \end{bmatrix} = \mathbf{J_B} \times \begin{bmatrix} \dot{x} \\ \dot{y} \\ \dot{z} \\ \dot{\alpha} \\ \dot{\beta} \\ \dot{\gamma} \end{bmatrix} \tag{23} $$

where

$$ \mathbf{J_A} = \begin{bmatrix} s\gamma + \sqrt{3}c\gamma & 0 & 0 \\ 0 & s\gamma + \sqrt{3}c\gamma & 0 \\ 0 & 0 & s\gamma + \sqrt{3}c\gamma \end{bmatrix} \tag{24} $$

$$ \mathbf{J_B} = \begin{bmatrix} J_{B11} & J_{B12} & 0 & 0 & 0 & J_{B16} \\ J_{B21} & J_{B22} & 0 & J_{B24} & J_{B25} & J_{B26} \\ J_{B31} & J_{B32} & 0 & J_{B34} & J_{B35} & J_{B36} \end{bmatrix} \tag{25} $$

See equation (26) below.

From equation (20), the length of the three prismatic legs of the tripod RPS can be differentiated and written as followed:

$$ \begin{aligned} q_{k+3}\dot{q}_{k+3} = \mathbf{c}_k\mathbf{d}_k{}^T\dot{\mathbf{o}}_2 + ({}^0_2\mathbf{R}.{}^2\mathbf{d}_k \times \mathbf{c}_k\mathbf{d}_k)^T\boldsymbol{\omega} - \mathbf{c}_k\mathbf{d}_k{}^T\mathbf{v}_1 \\ -(\mathbf{R}_z(\gamma)\,{}^1\mathbf{c}_k \times \mathbf{c}_k\mathbf{d}_k)^T\omega_1 \end{aligned} \tag{27} $$

where $\boldsymbol{\omega}$, $\boldsymbol{\omega_1}$ and $\mathbf{v}_1$ are respectively the angular velocity of the MP2 with respect to the fixed frame {O**xyz**}, the angular velocity and linear velocity of the MP1 with respect to the fixed frame {O**xyz**}.

Denoting that:

$$ \begin{cases} \boldsymbol{\rho}_k = \mathbf{c}_k\mathbf{d}_k = \left[\rho_{kx}, \rho_{ky}, \rho_{kz}\right]^T \\ \mathbf{c}_k = \mathbf{R}_z(\gamma)\,{}^1\mathbf{c}_k \times \mathbf{c}_k\mathbf{d}_k = \left[c_{kx}, c_{ky}, c_{kz}\right]^T \\ \mathbf{d}_k = {}^0_2\mathbf{R}\,{}^2\mathbf{d}_k \times \mathbf{c}_k\mathbf{d}_k = \left[d_{kx}, d_{ky}, d_{kz}\right]^T \end{cases} \tag{28} $$

$$ \begin{cases} J_{B11} = -2s\gamma \\ J_{B12} = 2c\gamma \\ J_{B16} = -r_a s\gamma - 2ys\gamma - 2xc\gamma + \sqrt{3}r_a c\gamma - q_1(c\gamma - \sqrt{3}s\gamma) \\ J_{B21} = s\gamma - \sqrt{3}c\gamma \\ J_{B22} = -c\gamma - \sqrt{3}s\gamma \\ J_{B24} = -\sqrt{3}r_b c\alpha s\beta \\ J_{B25} = -\sqrt{3}r_b s\alpha c\beta \\ J_{B26} = -r_a s\gamma + ys\gamma + xc\gamma - \sqrt{3}yc\gamma + \sqrt{3}xs\gamma + \sqrt{3}r_a c\gamma - q_2(c\gamma - \sqrt{3}s\gamma) \\ J_{B31} = s\gamma + \sqrt{3}c\gamma \\ J_{B32} = -c\gamma + \sqrt{3}s\gamma \\ J_{B34} = \sqrt{3}r_b c\alpha s\beta \\ J_{B35} = \sqrt{3}rbs\alpha c\beta \\ J_{B36} = -r_a s\gamma + ys\gamma + xc\gamma + \sqrt{3}yc\gamma - \sqrt{3}xs\gamma + \sqrt{3}r_a c\gamma - q_3(c\gamma - \sqrt{3}s\gamma) \end{cases} \tag{26} $$

Equation (35) can be written as followed:

$$q_{k+3}\dot{q}_{k+3} = \boldsymbol{\rho}_k{}^T\dot{\mathbf{o}}_2 + \mathbf{d}_k{}^T\boldsymbol{\omega} - \boldsymbol{\rho}_k{}^T\mathbf{v}_1 - \mathbf{c}_k{}^T\boldsymbol{\omega}_1 \tag{29}$$

By differentiating equation (17) with the time, the linear velocity $\mathbf{v_1} = [\dot{x}_1\ \dot{y}_1\ 0]^{\mathrm{T}}$ of MP1 with respect to the fixed reference coordinate $\{\mathbf{Oxyz}\}$ can be written as:

$$\mathbf{v}_1 = \begin{bmatrix} \dot{x} + (r_b c\alpha s\beta c\gamma)\dot{\alpha} + (r_b s\alpha c\beta c\gamma)\dot{\beta} - r_b s(\alpha s\beta s\gamma)\dot{\gamma} \\ \dot{y} + (r_b c\alpha s\beta s\gamma)\dot{\alpha} + (r_b s\alpha c\beta s\gamma)\dot{\beta} + (r_b s\alpha s\beta c\gamma)\dot{\gamma} \end{bmatrix} \tag{30}$$

Substituting equation (30) into equation (29) and some simple algebraic manipulation, yields:

$$\mathbf{J_C} \times \begin{bmatrix} \dot{q}_4 \\ \dot{q}_5 \\ \dot{q}_6 \end{bmatrix} = \mathbf{J_D} \times \begin{bmatrix} \dot{x} \\ \dot{y} \\ \dot{z} \\ \dot{\alpha} \\ \dot{\beta} \\ \dot{\gamma} \end{bmatrix} \tag{31}$$

where

$$\mathbf{J_C} = \begin{bmatrix} q_4 & 0 & 0 \\ 0 & q_5 & 0 \\ 0 & 0 & q_6 \end{bmatrix} \tag{32}$$

$$\mathbf{J_D} = \begin{bmatrix} 0 & 0 & J_{D13} & J_{D14} & J_{D15} & 0 \\ 0 & 0 & J_{D23} & J_{D24} & J_{D25} & 0 \\ 0 & 0 & J_{D33} & J_{D34} & J_{D35} & 0 \end{bmatrix} \tag{33}$$

See equation (34) below.

By combining equations (23) and (31), the Jacobean matrix can be expressed as:

$$\begin{bmatrix} \mathbf{J_A} & \mathbf{O}_{3\times 3} \\ \mathbf{O}_{3\times 3} & \mathbf{J_C} \end{bmatrix} \times \begin{bmatrix} \dot{q}_1 \\ \dot{q}_2 \\ \dot{q}_3 \\ \dot{q}_4 \\ \dot{q}_5 \\ \dot{q}_6 \end{bmatrix} = \begin{bmatrix} \mathbf{J_B} \\ \mathbf{J_D} \end{bmatrix} \times \begin{bmatrix} \dot{x} \\ \dot{y} \\ \dot{z} \\ \dot{\alpha} \\ \dot{\beta} \\ \dot{\gamma} \end{bmatrix} \tag{35}$$

where $\mathbf{0_{3\times 3}}$ is a zero matrix of 3 by 3.

The singular configurations of the mechanism are identified by using the Jacobian matrices to find the solution to the following equation:

$$\det(\mathbf{J}) = 0. \tag{36}$$

With $\mathbf{J}$, the mechanism Jacobian matrix.

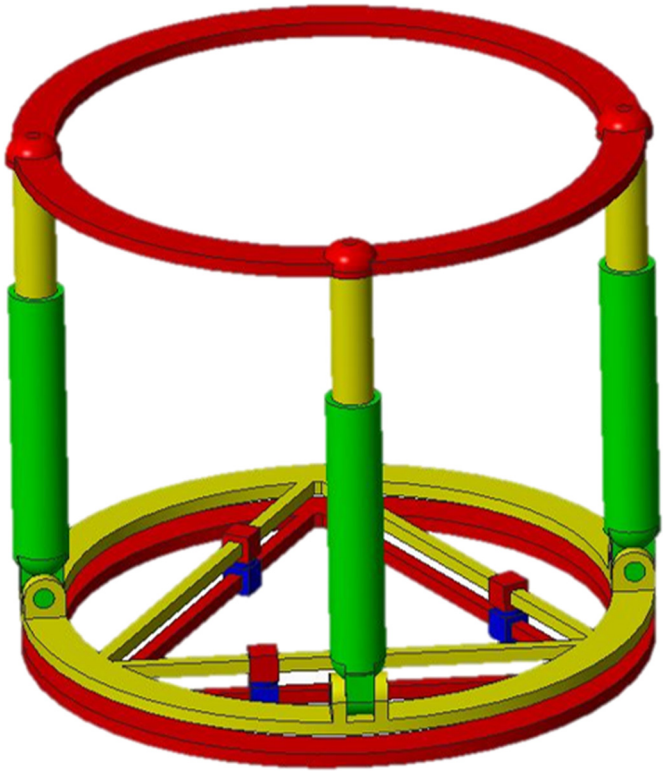

Fig. 4. The singular configuration of the planar parallel manipulator.

The singularity associated with the matrix $\mathbf{A}$ detailed in equation (35) is searched using equation (36).

$$\det(\mathbf{A}) = \left(s\gamma + \sqrt{3}c\gamma\right)^3 L_4 L_5 L_6 = 0. \tag{37}$$

By solving equation (37), it is found that the singularity will occur for a specific value of the angle γ that is show in the following equation:

$$\begin{cases} \gamma = \dfrac{2\pi}{3} + m2\pi \\ \gamma = -\dfrac{\pi}{3} + m2\pi \end{cases} \tag{38}$$

where m is an integer.

In the configuration given by equation (38), the planar mechanism will have its triangular base in the exact same orientation as the MP1. Therefore, the axes of both active and passive prismatic joints $\mathrm{R_k}$ and $\mathrm{R'_k}$ are collinear. This results infinite possible solutions of the inverse kinematic model as each active prismatic joint $\mathrm{R_k}$ could be located anywhere on their track. Which means that once in this configuration, operating the active joints q_1, q_2 and q_3 may not change the position of the MP1 in theory. This configuration is illustrated in Figure 4.

$$\begin{cases} J_{Dk3} = \rho_{kz} \\ J_{Dk4} = -(\rho_{kx}a_{11} + \rho_{ky}a_{21}) + d_{kx}c\gamma c\beta + d_{ky}s\gamma c\beta - s\beta(d_{kz} - c_{kz}) \\ J_{Dk5} = -(\rho_{kx}a_{12} + \rho_{ky}a_{22}) - d_{kx}s\gamma + d_{ky}c\gamma \end{cases} \tag{34}$$

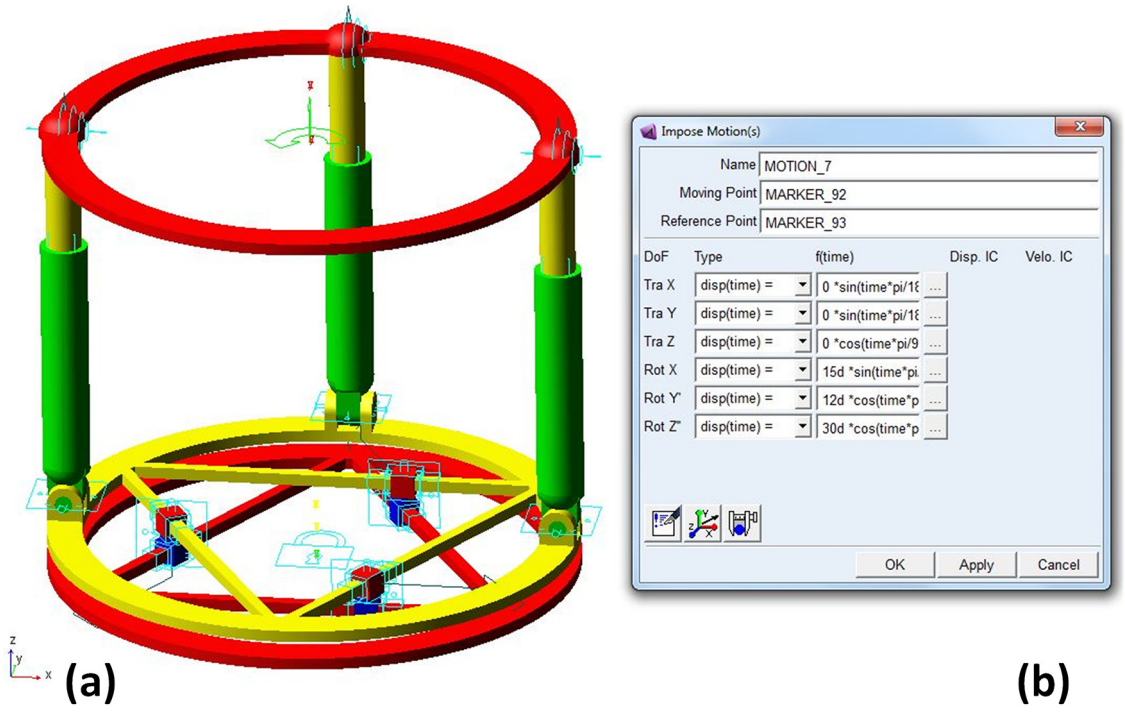

Fig. 5. Planar-Tripod Hydrid mechanism design and simulated in Adams.

Then, the singularity given by the matrix B is found as followed:

$$\det(\mathbf{B}) = 0. \tag{39}$$

The equation above will be verified when:

$$J_{B11}(J_{B26}J_{B32} - J_{B22}J_{B36}) + J_{B12}(J_{B21}J_{B36} - J_{B26}J_{B31}) + J_{B16}(J_{B22}J_{B31} - J_{B21}J_{B32}) = 0. \tag{40}$$

Substituting equations (17) and (26) into equation (40) yields:

$$J_{B16} + J_{B26} + J_{B36} = \frac{1 - c\left(\gamma + \frac{\pi}{3}\right)}{s\left(\gamma + \frac{\pi}{3}\right)} = 0 \tag{41}$$

If $s\left(\gamma + \frac{\pi}{3}\right) \neq 0$ or $\gamma \neq -\frac{\pi}{3} + m2\pi$ then $c\left(\gamma + \frac{\pi}{3}\right) \neq 1$

If $s\left(\gamma + \frac{\pi}{3}\right) = 0$ or $\gamma = -\frac{\pi}{3} + m2\pi$ then equation (41) becomes incompatible.

Therefore, the singularity will occur if $\gamma = -\frac{\pi}{3} + m2\pi$ (where m is an integer), which corresponds to the same configuration as identified by the equation (38).

4 Kinematic simulation on the mechanism

In order to verify the inverse kinematics and velocity models of the mechanism, a series of simulations have been carried out. The method consists generating a motion of the mechanism end effector given by the functions $x(t)$, $y(t)$, $z(t)$, $\alpha(t)$, $\beta(t)$ and $\gamma(t)$ and obtaining the corresponding evolution of the input variables *q1* to *q6*. Two groups of input variables are obtained by two different methods: one is obtained by implementing the mechanism input variables into the numerical simulation software Matlab, and another one by implementing the mechanism into the kinematic simulation software Adams. The resulting input variables groups are then compared. The Planar-Tripod Hydrid mechanism is designed in Adams software as seen in Figure 5a. Its inverse kinematic and velocity models are verified by generating a 6 DoF motion of the MP2, as illustrated in Figure 5b.

First, the impact of the parasitic motion generated by the tripod mechanism and the required motion compensation of the planar mechanism are tested. It is shown on Section 3.1 that the parasitic motion generates a displacement of the MP2 along the x axis of the reference frame $\{O_1\mathbf{x_1y_1z_1}\}$ as proven by equation (10). Projected on the $\{O\mathbf{xyz}\}$ reference frame, this motion is expressed as:

$$\begin{cases} x_{par} = -r_b s\alpha s\beta c\gamma \\ y_{par} = -r_b s\alpha s\beta s\gamma \end{cases} \tag{42}$$

In order to verify the kinematic model that compensate this parasitic motion, an angular motion of the MP2 is programmed in Adams. Meanwhile, a geometric constraint is added to fix the linear position of the MP2 by its center while all mechanism joints are set to remain passive. By using this method, the planar mechanism will automatically adjust its configuration to compensate the tripod parasitic motion. The resulting linear motion of the MP1 is then measured and compared to the parasitic motion compensation calculated via Matlab for the same MP2 angular motion. The motion component functions

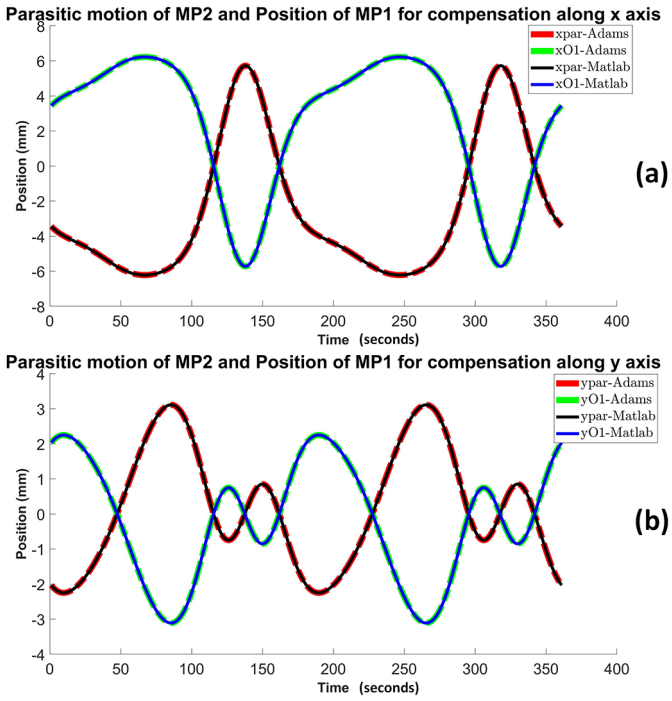

Fig. 6. MP2 parasitic motion and MP1 motion compensation along **x** axis (a) and **y** axis (b) calculated by Matlab and measured by Adams.

are input and defined as followed:

$$\begin{cases} x(t) = \text{TransX}(t) = 0 \\ y(t) = \text{TransY}(t) = 0 \\ z(t) = \text{TransZ}(t) = 0 \\ \alpha(t) = \text{RotX}(t) = \dfrac{\pi}{12}\sin(t) \\ \beta(t) = \text{RotY}(t) = \dfrac{\pi}{15}\sin(t) \\ \gamma(t) = \text{RotZ}(t) = \dfrac{\pi}{6}\cos(2t) \end{cases} \tag{43}$$

The parasitic motion of the MP2 and the compensation motion of the MP1 are calculated by Matlab and measured by Adams along the **x** and **y** axes and are respectively displayed in Figure 6a and b. According the graphic, no error can be found: not only the parasitic and compensation motions totally compensate each over, but their evolution resulting from Matlab and Adams are perfectly matched.

To verify the entire kinematic model, a trajectory is input in Adams and in Matlab. The MP2 motion component functions are defined as followed:

$$\begin{cases} x(t) = 20\sin(t) \\ y(t) = 20\sin(t) \\ z(t) = 50\cos(2t) \\ \alpha(t) = \dfrac{2\pi}{45}\sin(t) \\ \beta(t) = \dfrac{\pi}{18}\sin(t) \\ \gamma(t) = \dfrac{\pi}{12}\cos(2t) \end{cases} \tag{44}$$

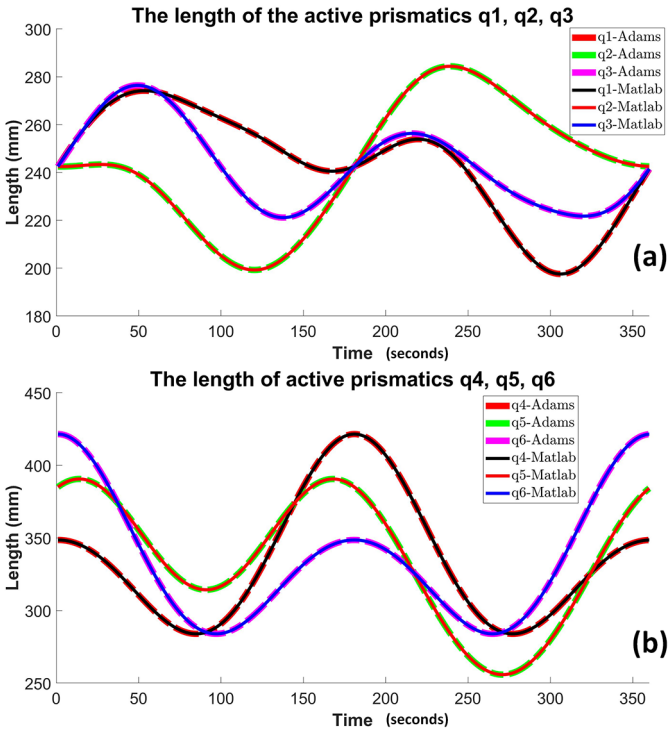

Fig. 7. Comparison of the mechanism input variables resulting from Adams and Matlab. (a) Input coordinates q_1, q_2, q_3. (b) Input coordinates q_4, q_5, q_6.

Then the evolution of the mechanism input variables corresponding to the motion described by equation (44) are measured in Adams and compared to the result given by Matlab. Both are displayed in Figure 7, showing no error between the two results. On the other hand, the velocity model of the mechanism is tested using the same method. The graphic in Figure 8 also shows no error between Adams and Matlab.

5 Mechanism workspace analysis

In this section, the workspace of the proposed mechanism is presented. There are various methods for calculating the workspace or boundaries of a mechanism such as using analytical, geometrical or numerical methods. This study uses a numerical method for determining the workspace boundaries of the hybrid planar-tripod mechanism manipulator. As the previously mentioned, this hybrid mechanism is made of one planar and one tripod mechanism, so the workspace analysis of the entire mechanism can be separated into two different studies. Therefore, the workspace of the mechanism is shown in two different coordinate systems: (x, y, γ) and (α, β, z) that are respectively associated with the planar and tripod mechanisms. A range of translational motion (x, y, z) and the orientation angles (α, β, γ) are discretized into sampling points with a desired resolution. For each point, two steps are required. First, the corresponding mechanism input variables (q_1,..., q_6) are calculated using the inverse kinematics model given by equations (17) and (21). Then

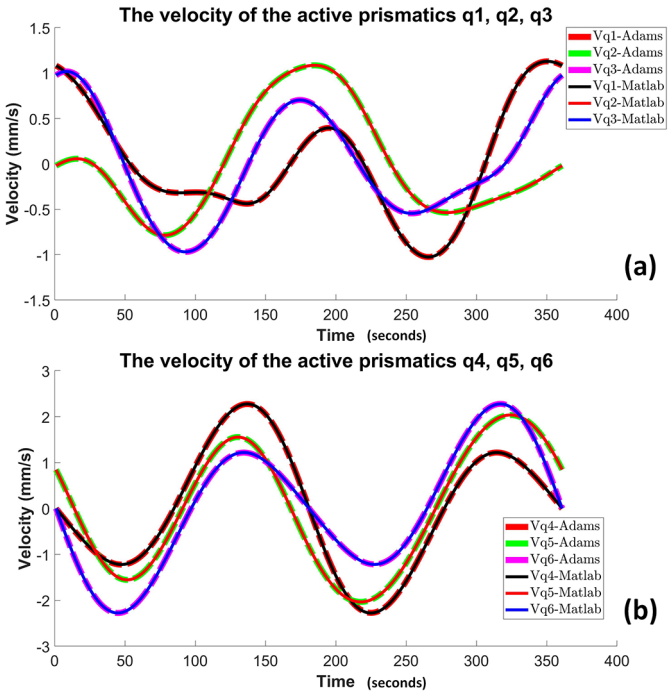

Fig. 8. Comparison of the mechanism input velocities resulting from Adams and Matlab. (a) Input velocities $\dot{q}_1, \dot{q}_2, \dot{q}_3$. (b) Input velocities $\dot{q}_4, \dot{q}_5, \dot{q}_6$.

the q_i values are checked to make sure they are within the stroke range limits given by $[\ q_{i\min}\ ;\ q_{i\max}]$. Second, if the sample point is considered inside the workspace, then it is required to determine whether all passive joints including revolute joints C_k and spherical joints D_k, are within their limits. The unit vectors perpendicular to the MP1 and along the axis of the spherical joints are respectively denoted $\mathbf{n_{rk}}$ and $\mathbf{n_{sk}}$ ($k = 1, 2, 3$). Then the constraints equations of revolute joints C_k and spherical joints D_k can be expressed as:

$$\begin{cases} \varphi_{rk} = \text{atan}\left(\dfrac{\mathbf{n_{rk}} \times \mathrm{C_kD_k}}{\mathbf{n_{rk}}.\mathrm{C_kD_k}}\right) \\ \varphi_{sk} = \text{atan}\left(\dfrac{\mathbf{n_{sk}} \times {}^{0}_{2}\mathbf{R}.\mathrm{C_kD_k}}{\mathbf{n_{sk}}.{}^{0}_{2}\mathbf{R}.\mathrm{C_kD_k}}\right) \end{cases} \tag{45}$$

$$\begin{cases} \varphi_{r\min} \leq \varphi_{rk} \leq \varphi_{r\max} \\ \varphi_{s\min} \leq \varphi_{sk} \leq \varphi_{s\max} \end{cases} \tag{46}$$

where $\varphi_{r\min}$, $\varphi_{r\max}$, $\varphi_{a\min}$, $\varphi_{a\max}$ are respectively the minimum and maximum working angles of revolute and spherical joints.

If the values φ_{rk} and φ_{sk} are suitable for constraints given by equation (45), then the passive joints are within their allowable range. Which means the considered point is a reachable by the mechanism. In order to study the suitability of the proposed hybrid planar-tripod mechanism with bone reduction surgery, its workspace is compared to the Stewart platform which is the most commonly used architecture in the medical application. To ensure a fair comparison, the Stewart platform and the hybrid mechanism are set with the same general dimensions as illustrated in Figure 9. Their input variables range of motion are also adjusted similarly. The associated parameters are displayed in Table 1.

Table 1. Geometric and motion parameters of the hybrid mechanism and Stewart platform.

Variable	Value	Variable	Value
r_a (mm)	190	$\varphi_{r\ \min}$ (deg)	–45
r_b (mm)	190	$\varphi_{r\ \max}$ (deg)	45
$q_{\min}$ (mm)	175	$\varphi_{s\ \min}$ (deg)	–20
$q_{\max}$ (mm)	250	$\varphi_{s\ \max}$ (deg)	20

For each mechanism, the (x, y, γ) and (α, β, z) coordinate system workspaces are respectively displayed in Figures 10 and 11. As shown in Table 2, it reveals that while the maximum (xy) planar motion range is at $\gamma = 0$ for the Steward platform, it is around $\gamma = 23$ degrees for the hybrid mechanism. In this configuration, the motion range of the hybrid mechanism is 17% larger on **x** axis and 13% larger on the **y** axis, while the Steward platform has vertical motion range 3% larger. Although the Steward platform angular motion is 21% larger on angle β, the hybrid mechanism has an angular motion 16% larger on angle α and 162% larger on angle γ. As shown in Figure 10, the major contribution of the proposed mechanism is to significantly increase the range of the bone longitudinal rotation, even when it is located away from the workspace center.

As a result, the above kinematic simulations show that the proposed mechanism has a better workspace that the standard Stewart platform. On addition, it is capable of generating a much larger range of longitudinal rotation at a deported linear position (x, y). So the hybrid mechanism has enhanced capacities in providing fracture surface matching while the Steward platform would experience difficulties in this regard. This issue could be solved by determining an accurate initial position for the Steward manipulator that would ascertain a complete trajectory remaining within its workspace. However, the existence of such a position is not guaranteed since its workspace is limited. Also, in the case such a position exists, an accurate and delicate registration of the manipulator with the bone fragments would be required. This confirms the importance of designing a mechanism that generate a larger workspace and a more adapted kinematic. When using the proposed hybrid mechanism, registration aspects will be less of a concern since its workspace is significantly improved.

6 Conclusions

In the present study, a new hybrid architecture is proposed for bone reduction surgery. It is defined as a 3-$\underline{\text{P}}$RP planar mechanism which is attached with a 3-R$\underline{\text{P}}$S tripod mechanism. The kinematic and velocity models of the

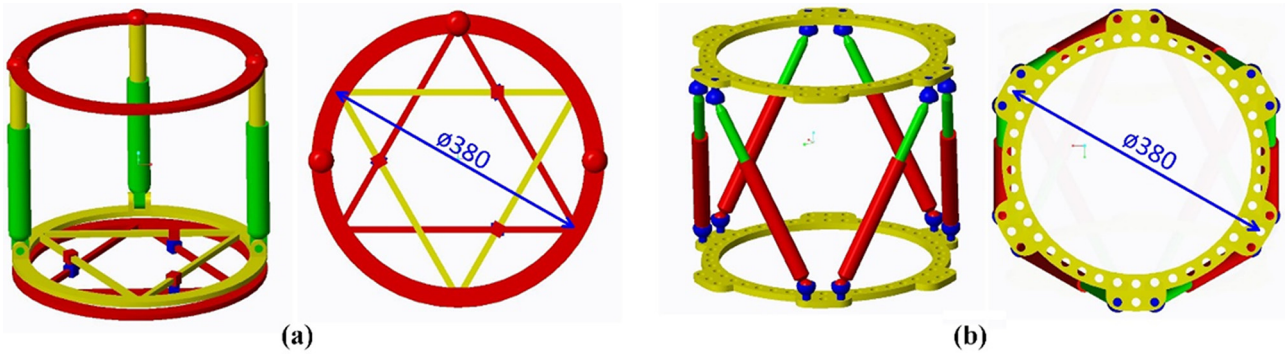

Fig. 9. (a) The proposed hybrid robot. (b) Stewart platform.

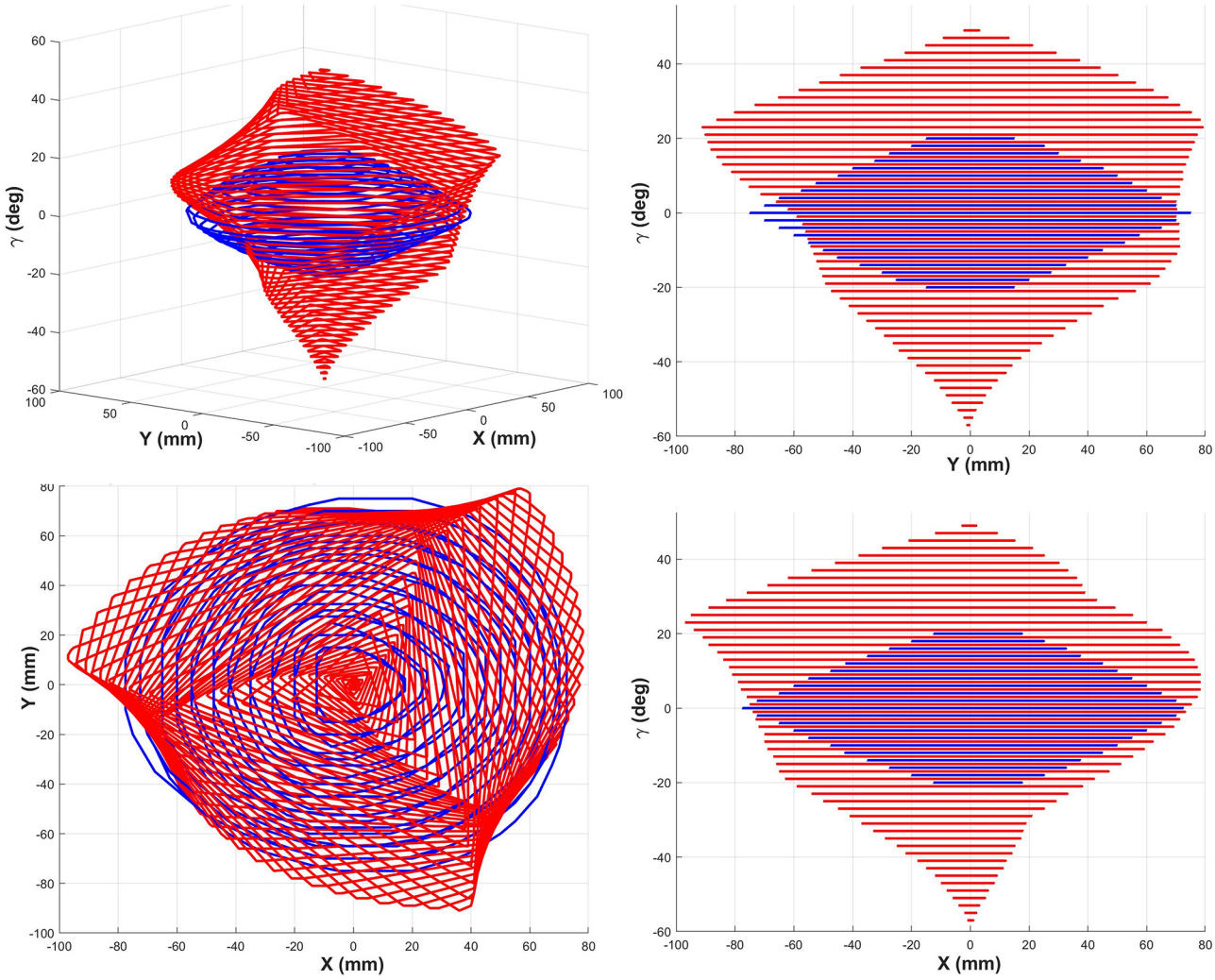

Fig. 10. Workspace representation of the hybrid mechanism (red) and the Stewart platform (blue) in the (x, y, γ) coordinate system.

Table 2. Hybrid mechanism and Steward platform workspace dimension ranges.

Workspace dimensions	Δx (mm)	Δy (mm)	Δz (mm)	$\Delta\alpha$ (deg)	$\Delta\beta$ (deg)	$\Delta\gamma$ (deg)
Hybrid mechanism	175	170	75	37	22	105
Steward platform	150	150	77	32	28	40
Improvement	+17%	+13%	–3%	+16%	–21%	+162%

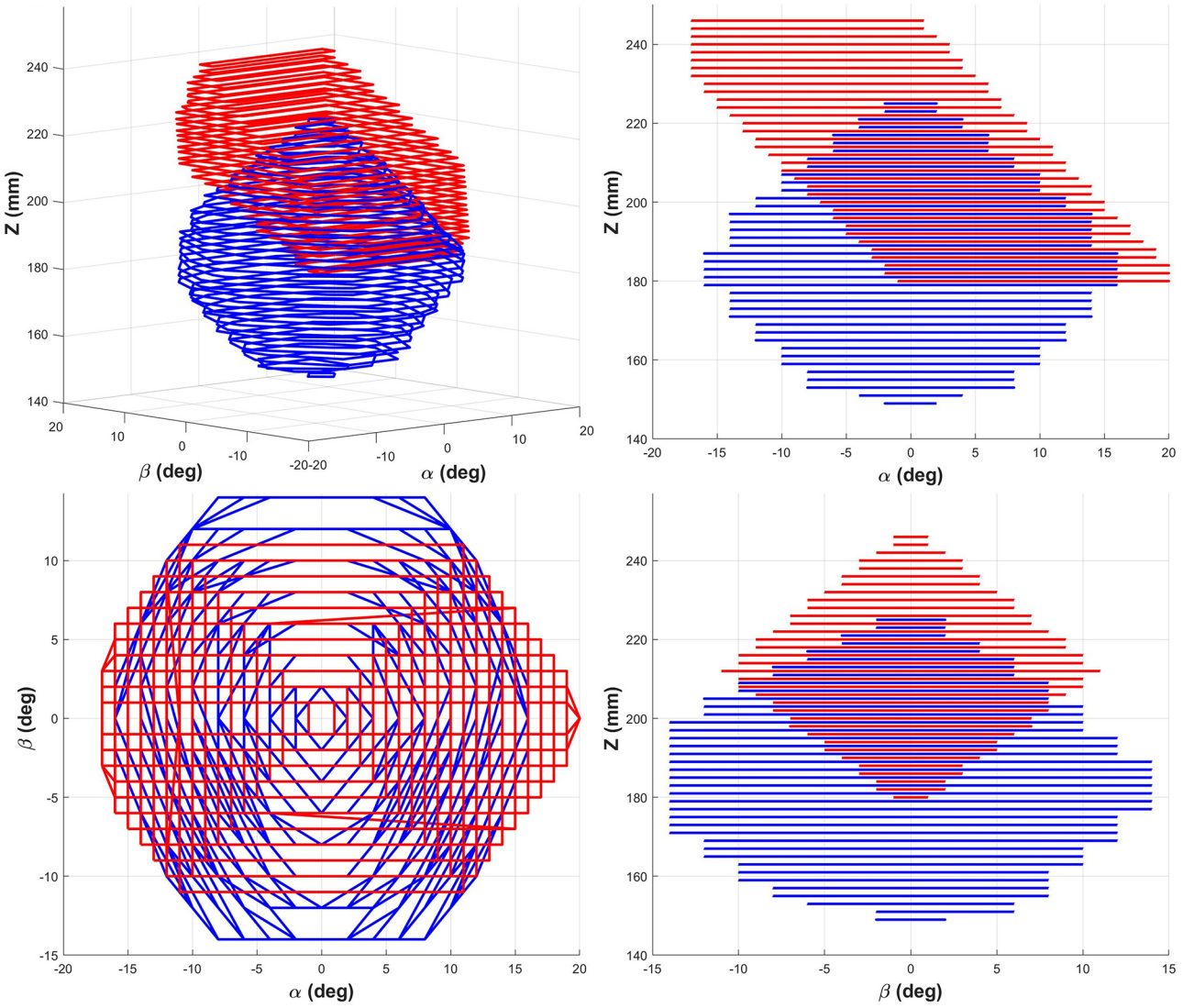

Fig. 11. Workspace representation of the hybrid mechanism (red) and the Stewart platform (blue) in the (α, β, z) coordinate system.

entire mechanism is provided. The parasitic motion generated by the tripod mechanism end effector rotation is also considered. Due to its specific architectural arrangement, this parasitic motion is generated on only one axis of the tripod base. Also, the kinematic model of the planar mechanism is defined to provide a total compensation of the parasitic motion on both axes of the entire mechanism base. A series of kinematic simulations has allowed the validation of the mechanism kinematic and velocity models and has demonstrated the compensation of the parasitic motion, showing the correctness of this study. The workspace analysis of the hybrid planar-tripod mechanism has shown that it is able to cover a larger workspace than the classical Taylor mechanism that is mostly used in this surgical application. Which makes the hybrid planar-tripod mechanism a better candidate for bone reduction surgery.

References

[1] T.L. Arneson, L.J. Melton, D.G. Lewallen, W.N. O'Fallon, Epidemiology of diaphyseal and distal femoral fractures in Rochester, Minnesota, 1965–1984, Clin. Orthopaed. Related Res. **234**, 188–194 (1998)

[2] M. Zlowodzki, M. Bhandari, D.J. Marek, P.A. Cole, P.J. Kregor, Operative treatment of acute distal femur fractures: systematic review of 2 comparative studies and 45 case series (1989 to 2005), J. Orthopaedic Trauma **20**, 366–371 (2006)

[3] D.J. Johnstone, W.J.P. Radford, E.J. Parnell, Interobserver variation using the AO/ASIF classification of long bone fractures, Injury **24**, 163–165 (1993)

[4] D.M. Kahler, Navigated long-bone fracture reduction, J. Bone Joint Surg. **91**, 102–107 (2006)

[5] G.A. Ilizarov, V.I. Ledyaev, The replacement of long tubular bone defects by lengthening distraction osteotomy of one of the fragments, Clin. Orthop. Related Res. **280**, 7–10 (1992)

[6] K. Seide, D. Wolter, H.R. Kortmann, Fracture reduction and deformity correction with the hexapod Ilizarov fixator, Clin. Orthopaed. Related Res. **363**, 186–195 (1999)
[7] L.N. Solomin, D. Paley, E.A. Shchepkina, V.A. Vilensky, P. V. Skomoroshko, A comparative study of the correction of femoral deformity between the Ilizarov apparatus and Ortho-SUV Frame, Int. Orthopaed. **38**, 865–872 (2013)
[8] P.V. Skomoroshko, V.A. Vilensky, A.I. Hammouda, M.D.A. Fletcher, L.N. Solomin, Mechanical rigidity of the Ortho-SUV frame compared to the Ilizarov frame in the correction of femoral deformity, Strat. Trauma Limb Reconstruc. **10**, 5–11 (2015)
[9] K. Seide, M. Faschingbauer, M.E. Wenzl, N. Weinrich, C.A. Juergens, A hexapod robot external fixator for computer assisted fracture reduction and deformity correction, Int. J. Med Robot. Comput. Assist. Surg. **1**, 64–69 (2004)
[10] D. Keshet, M. Eidelman, Clinical utility of the Taylor spatial frame for limb deformities, Orthop. Res. Rev. **9**, 51–61 (2017)
[11] R.D. Gregorio, V. Parenti-Castelli, Kinematics of a six-dof fixation device for long-bone fracture reduction, J. Robotic Syst. **18**, 715–722 (2001)
[12] R.D. Gregorio, V. Parenti-Castelli, Fixation devices for long bone fracture reduction: an overview and new suggestions, J. Intell. Robot. Syst. **34**, 265–278 (2002)
[13] J.C. Taylor, Perioperative planning for two- and three-plane deformities, Foot Ankle Clinics **13**, 69–121 (2008)
[14] M.J. Al-Sayyad, Taylor spatial frame in the treatment of pediatric and adolescent tibial shaft fractures, J. Pediat. Orthopaed. **26**, 164–170 (2006)
[15] P. Tang, L. Hu, H. Du, M. Gong, L. Zhang, Novel 3D hexapod computer-assisted orthopaedic surgery system for closed diaphyseal fracture reduction, Int. J. Med. Robot. Comput Assist. Surg. **8**, 17–24 (2012)
[16] T. Wang, C. Li, L. Hu, P. Tang, L. Zhang, H. Du, S. Luan, L. Wang, Y. Tan, C. Peng, A removable hybrid robot system for long bone fracture reduction, Bio-Medical Mater. Eng. **24**, 501–509 (2014)
[17] M.H. Abedinnasab, J. Gallardo-Alvarado, F. Farahmand, A wide-open 3-legged parallel robot for long bone fracture reduction, J. Mech. Robot. **9**, 015001 (2017)
[18] C.I. Moorroft, P.B.M. Thomas, P.J. Ogrodnick, S.A. Verborg, A device for improved reduction of tibial fractures treated with external fixation, Proc. Inst. Mech. Eng. H **214**, 449–457 (2000)
[19] Y.H. Kim, I. Nozomu, E.Y.S. Chao, Kinematic simulation of fracture reduction and bone deformity correction under unilateral external fixation, J. Biomech. **35**, 1047–1058 (2002)
[20] T.K.K. Koo, E.Y.S. Chao, A.F.T. Mak, Development and validation of a new approach for computer-aided long bone fracture reduction using unilateral external fixator, J. Biomech. **39**, 2104–2112 (2006)
[21] T.K.K. Koo, A.F.T. Mak, A knowledge-based computer-aided system for closed diaphyseal fracture reduction, Clin. Biomech. **22**, 884–893 (2007)
[22] B. Füchtmeier, S. Egersdoerfer, R. Mai, R. Hente, D. Dragoi, G. Monkman, M. Nerlich, Reduction of femoral shaft fractures in vitro by a new developed reduction robot system 'RepoRobo', Int. J. Care Injured **35**, 113–119 (2004)
[23] R. Westphal, T. Gösling, M. Oszwald, J. Bredow, D. Klepzig, S. Winkelbach, T. Hüfner, C. Krettek, F. Wahl, Robot assisted fracture reduction, Exp. Robot. **39**, 153–163 (2008)
[24] S. Joung, H. Kamon, H. Liao, J. Iwaki, T. Nakazawa, M. Mitsuishi, Y. Nakajima, T. Koyama, N. Sugano, Y. Maeda, M. Bessho, S. Ohshi, T. Matsumoto, I. Ohinshi, I. Sakuma, A robot assisted hip fracture reduction with a navigation system, Med. Image Comput. Comput. Assist. Intervent. **5242**, 501–508 (2008)
[25] A.E. Graham, S.Q. Xie, K.C. Aw, W.L. Xu, S. Mukherjee, Robotic long bone fracture reduction, Medical Robotics, IntechOpen, 2008.
[26] H. Du, L. Hu, C. Li, T. Wang, L. Zhao, Y. Li, Z. Mao, D. Liu, L. Zhang, C. He, L. Zhang, H. Hou, L. Zhnag. P. Tamg, Advancing computer-assisted orthopaedic surgery using a hexapod device for closed diaphyseal fracture reduction, Int. J. Med. Robot. Comp. Assist. Surg. **11**, 348–359 (2015)
[27] M. Daniali, H.P. Zsombor-Murray, P.J. Angeles, The kinematics of 3-DoF planar and spherical double-triangular parallel manipulators, Comput. Kinem. Solid Mech. Appl. **28**, 153–164 (1993)
[28] K.H. Hunt, Structural kinematics of in-parallel-actuated robot-arms, J. Mech. Trans. Autom. Design **105**, 705–712 (1983)
[29] Q. Li, Z. Chen, Q. Chen, C. Wu, X. Hu, Parasitic motion comparison of 3-PRS parallel mechanism with different limb arrangements, Robot. Comput. Integr. Manufact. **27**, 389–396 (2011)

Cite this article as: T. Essomba, S.N. Phu, Kinematic design of a hybrid planar-tripod mechanism for bone reduction surgery, Mechanics & Industry **21**, 403 (2020)